Science Bulletin xxx (xxxx) xxx

Contents lists available at ScienceDirect

Science Bulletin

journal homepage: www.elsevier.com/locate/scib

www.scibull.com

Article

Scaling analysis of quantum geometry in second-order nonlinear transport

Zhen-Hao Gong [a,1], Z.Z. Du [a,b,1], Hai-Peng Sun [c], Hai-Zhou Lu [a,b,*], X.C. Xie [d,e,f]

[a] State Key Laboratory of Quantum Functional Materials, Department of Physics, Guangdong Provincial Key Laboratory of Topological Matter, and Guangdong Basic Research Center of Excellence for Quantum Science, Southern University of Science and Technology (SUSTech), Shenzhen 518055, China
[b] Quantum Science Center of Guangdong-Hong Kong-Macao Greater Bay Area (Guangdong), Shenzhen 518045, China
[c] Shenzhen Key Laboratory of Ultraintense Laser and Advanced Material Technology, Center for Intense Laser Application Technology, and College of Engineering Physics, Shenzhen Technology University, Shenzhen 518118, China
[d] Interdisciplinary Center for Theoretical Physics and Information Sciences (ICTPIS), Fudan University, Shanghai 200433, China
[e] International Center for Quantum Materials, School of Physics, Peking University, Beijing 100871, China
[f] Hefei National Laboratory, Hefei 230088, China

A R T I C L E I N F O

Article history:
Received 1 June 2026
Received in revised form 20 June 2026
Accepted 16 July 2026
Available online xxxx

Keywords:
Quantum geometry
Nonlinear Hall effect
Disorder
Quantum metric
Scaling law

A B S T R A C T

Quantum geometry encodes the structure of the Hilbert space of Bloch states and can be accessed through nonlinear transport. Yet, disorder-induced mechanisms generically contribute to nonlinear transport, making it difficult to isolate quantum-geometric contributions in experiments. Here we systematically enumerate geometric and disorder-induced mechanisms of the second-order nonlinear Hall effect and derive a scaling law that expresses the nonlinear Hall conductivity as a polynomial of the linear longitudinal conductivity. Crucially, each mechanism carries a distinct "weight fingerprint" in the polynomial, enabling a quantitative disentanglement of quantum geometry from disorder backgrounds in existing experiments, both with and without time-reversal symmetry. Our results provide an implementable workflow for identifying quantum-geometric contributions in nonlinear-transport measurements.

1. Introduction

The nonlinear Hall effect manifests as a transverse voltage nonlinearly dependent on the longitudinal driving current (Fig. 1a) [1–11]. It has attracted broad interest due to its potential as a spectroscopic tool [12–30] and in device applications such as wireless rectification [31,32], as well as its connections to nonlinear optics [33–36]. Notably, the second-order response can originate from the quantum metric [1,8,9] and Berry curvature [2,3,5], which correspond to the real and imaginary parts of quantum geometry, respectively [37–45]. Quantum geometry quantifies distances between quantum states and can provide geometric insights into challenges in condensed matter [46], in particular in the fractional Chern insulator [39–41] and flat-band superconductivity [42,43]. Disorder can also reshape band topology and drive quantum phase transitions, as demonstrated by disorder-induced nodal-knot transitions [47]. However, disorder-induced mechanisms, such as side jump (SJ) that shifts coordinates of electrons sideways and skew scattering (SK) that asymmetrically deflects electrons (Fig. 1b) [48], are often comparable and must be accounted for in the nonlinear transport [12,31,33,49,50]. Therefore, a central open issue is how to unambiguously identify quantum geometry from the disorder-induced mechanisms, despite a huge amount of experimental data.

In this work, we derive the formulas for all possible mechanisms of second-order nonlinear transport by treating geometry and disorder on an equal footing. The formulas allow us to derive a scaling law that expresses the nonlinear Hall conductivity as a polynomial function of the linear longitudinal conductivity. More importantly, we find each mechanism has a distinct weight distribution of the polynomial terms, which allows us to identify quantum geometry from disorder-induced mechanisms in the recent experiments with and without $\mathscr{T}$ symmetry. The formulas also allow us to determine nonzero nonlinear conductivity elements for materials categorized by the magnetic point groups. Our theory is not only a comprehensive description of the second-order non-

* Corresponding author.
E-mail address: luhz@sustech.edu.cn (H.-Z. Lu).
[1] These authors contributed equally to this work.

https://doi.org/10.1016/j.scib.2026.07.062
2095-9273/

Please cite this article as: Z.-H. Gong, Z.Z. Du, H.-P. Sun et al., Scaling analysis of quantum geometry in second-order nonlinear transport, Science Bulletin, https://doi.org/10.1016/j.scib.2026.07.062

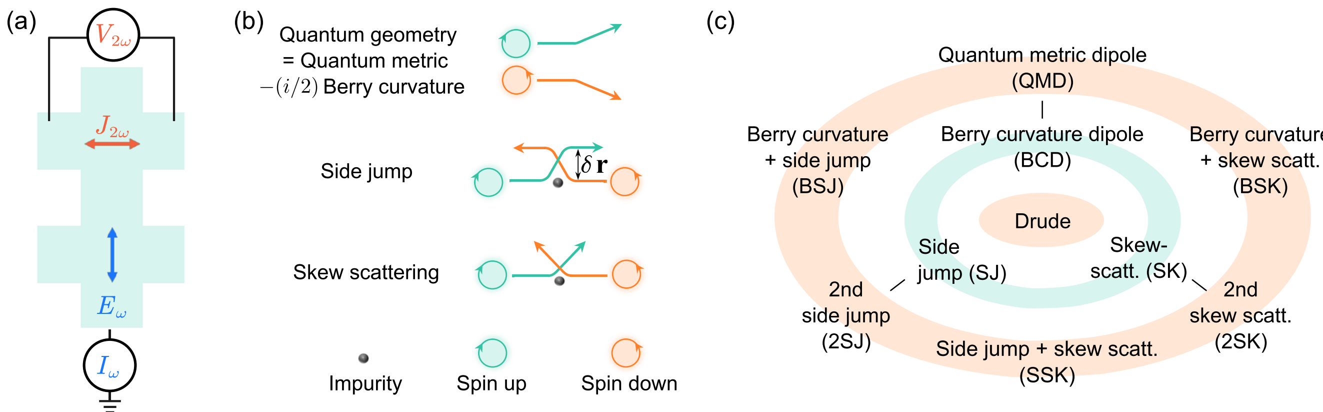

Fig. 1. Mechanisms of the second-order nonlinear transport. (a) Nonlinear Hall effect is measured experimentally as a double-frequency transverse voltage $V_{2\omega}$ driven by a low-frequency current I_ω (10–1000 Hz), or calculated theoretically as a current density $J_{2\omega}$ driven by an electric field E_ω. (b) The building blocks for the nonlinear transport, including quantum geometry (= quantum metric $-i/2$ Berry curvature), SJ (which induces a lateral coordinate shift of spin-up and spin-down electrons oppositely by $\delta\mathbf{r}$), and SK (which asymmetrically deflects spin-up and spin-down electrons). (c) Hierarchy of the second-order nonlinear transport. (i) The Berry curvature dipole (BCD) [2,3], SJ, and SK mechanisms [12,14] survive time-reversal ($\mathscr{T}$) symmetry, require broken spatial inversion ($\mathscr{P}$) symmetry, and are forbidden by $\mathscr{P}\mathscr{T}$ symmetry. (ii) The Drude, quantum metric dipole (QMD) [1,8,9] mechanisms as well as second-order skew scattering (2SK), second-order side jump (2SJ), side-jump-plus-skew-scattering (SSK), Berry-curvature-plus-side-jump (BSJ), and Berry-curvature-plus-skew scattering (BSK), part of which has been known as the anomalous skew scattering [33], require broken $\mathscr{T}$ and $\mathscr{P}$ symmetries but survive the combined $\mathscr{P}\mathscr{T}$ symmetry.

linear transport, but also provides a quantitative tool and implementable workflow for identifying quantum-geometry–driven nonlinear responses in future experiments and applications.

2. Mechanisms of second-order nonlinear transport

A Hall effect occurs when electrons driven by an electric field are deflected to the transverse direction. In the absence of an external magnetic field, three mechanisms may lead to the Hall effect linear in electric field $\vec{E}$: Berry curvature, SJ, and SK [48], as shown in Fig. 1b. The Berry curvature [51] describes the curvature of the Hilbert space of the Bloch states, which thereby prevents electrons from moving straight in a perfect crystal. Moreover, the Berry-curvature contribution itself acquires an electric-field-induced geometric correction, governed by the quantum metric [1,8,9]. In the presence of disorder, that is, imperfection of the crystal, SJ shifts the coordinates of spin-up and spin-down electrons sideways in opposite directions, and SK asymmetrically deflects spin-up and spin-down electrons due to the spin–orbit coupling. These mechanisms and mixing of them can capture all contributions up to second order in the electric field (i.e., $\propto E^2$) within the semiclassical framework. The hierarchy of all mechanisms for the nonlinear Hall effect is categorized in Fig. 1c according to three different symmetries, i.e., the $\mathscr{T}$, $\mathscr{P}$, and combined $\mathscr{P}\mathscr{T}$ symmetries.

Experimentally, the nonlinear Hall effect is measured as a double-frequency transverse voltage in response to a low-frequency current (10–1000 Hz). Theoretically, the nonlinear conductivity χ_{abc} is defined in terms of the double-frequency current density

$$J_a(2\omega) = \chi_{abc}E_b(\omega)E_c(\omega), \tag{1}$$

in response to low-frequency electric fields $E_b(\omega)$ and $E_c(\omega)$, where ω is the frequency, $a, b, c \in \{x, y, z\}$. χ_{abc} can be calculated using the semiclassical theory to treat quantum geometry (including the Berry curvature and quantum metric) and disorder on an equal footing. We find that the second-order nonlinear conductivity χ_{abc} can be decomposed as

$$\begin{aligned}\chi_{abc} = \; & \chi^{\mathrm{Drude}} \\ & + \chi^{\mathrm{BCD}} + \chi^{\mathrm{SJ}} + \chi^{\mathrm{SK}} \\ & + \chi^{\mathrm{QMD}} + \chi^{\mathrm{2SK}} + \chi^{\mathrm{2SJ}} + \chi^{\mathrm{SSK}} + \chi^{\mathrm{BSJ}} + \chi^{\mathrm{BSK}},\end{aligned} \tag{2}$$

where $\chi^{\mathrm{2SK}}, \chi^{\mathrm{2SJ}}, \chi^{\mathrm{SSK}}, \chi^{\mathrm{BSJ}}$, and part of χ^{BSK} are derived in this work, complementing five previously known mechanisms [1–3,8,9,12,31,33,50]. Among the mechanisms, quantum metric dipole (QMD) and Berry curvature dipole (BCD) are particularly notable as they directly probe quantum geometry that measures the distance between quantum states. All terms on the first line of Eq. (2) have the same symmetry under which the quantum metric emerges in the nonlinear transport. The derivation, explicit formulas, and symmetries of the mechanisms can be found in Section 4.

3. Identification of nonlinear transport mechanisms

3.1. Scaling law of second-order nonlinear transport

Because disorder-induced mechanisms are present, quantitatively identifying the quantum-geometry contributions to nonlinear transport remains challenging. Scaling laws have proven successful in distinguishing mechanisms in linear Hall effects [48,52,53]. We derive a scaling law for the second-order nonlinear transport as a polynomial relation between the transverse nonlinear Hall conductivity χ_{yxx} and longitudinal linear conductivity σ_{xx}

$$\chi_{yxx} = \mathscr{C}_4\sigma_{xx}^4 + \mathscr{C}_3\sigma_{xx}^3 + \mathscr{C}_2\sigma_{xx}^2 + \mathscr{C}_1\sigma_{xx} + \mathscr{C}_0, \tag{3}$$

where in experiments $\chi_{yxx} = V_y^{2\omega}\sigma_{xx}L^2/(V_x^{\omega})^2W$, L is the length, W is the width in two-dimensional (2D) systems or cross-sectional area in 3D systems, $V_y^{2\omega}$ is the transverse double-frequency voltage, and V_x^{ω} is the longitudinal single-frequency voltage. The scaling law is also found for $\mathscr{T}$-odd nonlinear Hall effect [50]. In this work, we further find distinct weight distributions of the $\mathscr{C}_i\sigma_{xx}^i$ terms for all the mechanisms, as shown in Table 1, which could serve as signatures to distinguish the mechanisms in experiments. Except that the BSK and 2SJ mechanisms have the same weight distribution, the remaining 8 out of 10 mechanisms have unique weight distributions, such as QMD or 2SK. The workflow of identifying the mechanisms is as follows: (i) fitting χ_{yxx} as a polynomial of σ_{xx} using Eq. (3) and (ii) identifying the underlying mechanisms by matching the fitted weights to Table 1.

In Fig. 2 we present the fitting results for a series of experiments on $MnBi_2Te_4$ thin films [10,11,54], which preserve $\mathscr{P}\mathscr{T}$ symmetry; therefore, QMD is expected to dominate the nonlinear Hall effect.

Table 1
Weights of the polynomial terms in the scaling law Eq. (3) for each of the mechanisms of the second-order nonlinear Hall effect in Fig. 1.

Mechanism	$\mathscr{C}_4\sigma_{xx}^4$	:	$\mathscr{C}_3\sigma_{xx}^3$	:	$\mathscr{C}_2\sigma_{xx}^2$	:	$\mathscr{C}_1\sigma_{xx}$	:	$\mathscr{C}_0$
Drude	0	:	0	:	1	:	0	:	0
BCD*	0	:	0	:	0	:	1	:	0
SJ*	0	:	0	:	1	:	−1	:	0
SK*	0	:	1	:	−2	:	1	:	0
QMD	0	:	0	:	0	:	0	:	1
BSJ	0	:	0	:	0	:	1	:	−1
2SK	1	:	−4	:	6	:	−4	:	1
SSK	0	:	1	:	−3	:	3	:	−1
BSK, 2SJ	0	:	0	:	1	:	−2	:	1

The mechanisms without (with) an asterisk (do not) require broken $\mathscr{T}$ symmetry.

Fig. 2a and b are for a 6-septuple-layer $MnBi_2Te_4$ thin film strained by black phosphorus [10]. The fitting shows a dominant $\mathscr{C}_0$ term, indicating the dominance of QMD in this experiment according to Table 1. Fig. 2c–f are for two devices of 6-septuple-layer $MnBi_2Te_4$ [11,54] in the absence of the black phosphorus. In both devices, the mechanisms are found to be from both QMD and a disorder-induced Drude mechanism, although the two devices are quite different in the magnitudes of the linear longitudinal and second-order Hall conductivities. Fig. 2g and h are for a 4-septuple-layer $MnBi_2Te_4$ thin film [11], which indicates that Drude and QMD are the dominant mechanisms, while 2SJ, 2SK, and SSK make only minor contributions.

The substantially different dominant mechanisms in the devices could be understood in terms of their symmetries. The unstrained $MnBi_2Te_4$ thin film has a threefold rotational C_3 symmetry, which can be broken by strain. The C_3 symmetry forbids geometric mechanisms [12], including the BCD and QMD mechanisms. The 6-septuple-layer devices in the absence of black phosphorus likely experience extrinsic C_3 symmetry breaking (e.g., substrate-induced strain or inhomogeneity), allowing QMD to emerge as one of the dominant mechanisms. In summary, the fitting results in Fig. 2 support QMD as the dominant mechanism of nonlinear Hall effect in most devices.

We also apply the scaling law to $\mathscr{T}$-even devices to identify the BCD mechanism. Fig. 3 shows the fitting results for two devices of

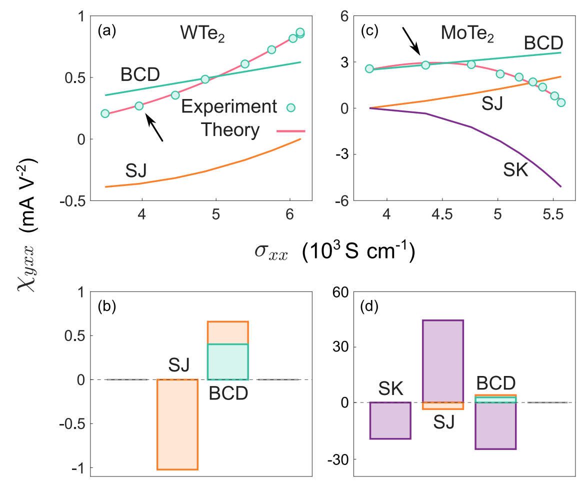

Fig. 3. Scaling analysis of the mechanisms for the nonlinear Hall effect in $\mathscr{T}$-even systems. (a) Fitted nonlinear Hall conductivity χ_{yxx} (red solid curve) as a function of the linear longitudinal conductivity σ_{xx} for the experimental data (circles) of a device of WTe_2 in the temperature range $T = 2$–100 K [6]. (b) Weights of the five $\mathscr{C}_i\sigma_{xx}^i$ terms in Eq. (3) for the data from (a) at $\sigma_{xx} = 3.96 \times 10^3$ S cm^{-1} (indicated by the arrow). (c and d) For a device of $MoTe_2$ in the temperature range $T = 2.5$–100 K [55].

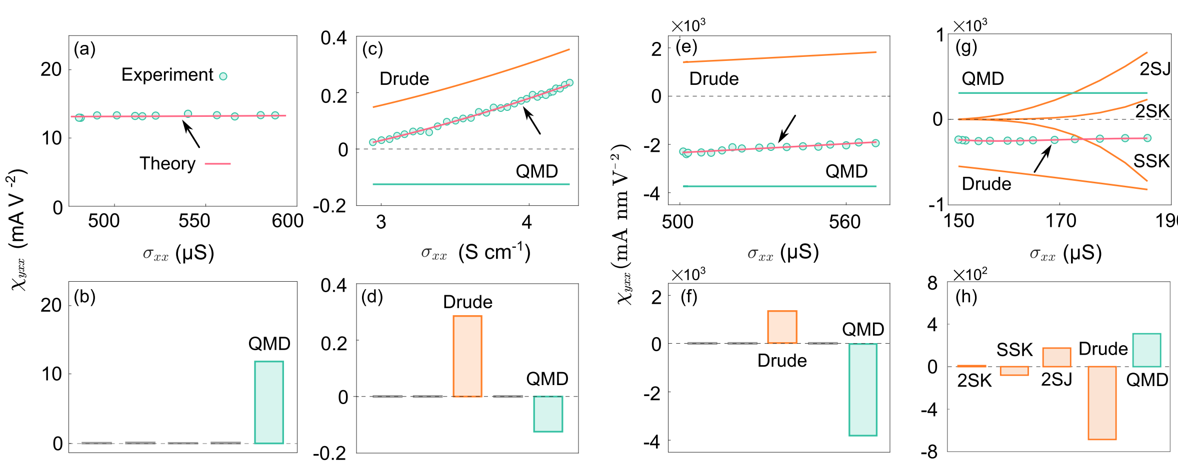

Fig. 2. Scaling analysis of the mechanisms for the nonlinear Hall effect in $MnBi_2Te_4$ thin films. (a) Fitted nonlinear Hall conductivity χ_{yxx} (red solid curve) as a function of the linear longitudinal conductivity σ_{xx}, for the experimental data (circles) of a 6-septuple-layer $MnBi_2Te_4$ thin film strained by black phosphorus in the temperature range $T = 2$–13 K [10]. (b) Weights of the five $\mathscr{C}_i\sigma_{xx}^i$ terms in Eq. (3) for the data from (a) at $\sigma_{xx} = 540$ μS (indicated by the arrow). (c and d) For a 6-septuple-layer $MnBi_2Te_4$ thin film without phosphorus in the temperature range $T = 2$–20 K [54]. (e and f) For a 6-septuple-layer $MnBi_2Te_4$ thin film without phosphorus in the temperature range $T = 2$–10 K [11]. (g and h) For a 4-septuple-layer $MnBi_2Te_4$ thin film in the temperature range $T = 1.6$–10 K [11]. In (h), the weight of the QMD mechanism is multiplied by 200 times for demonstration and non-QMD is the summation of the weights of the 2SJ, 2SK, SSK, and Drude mechanisms. Different from other panels, the weights in (h) are not displayed in terms of the polynomials of σ_{xx} but in terms of the mechanisms.

Table 2
Symmetry-allowed components of the nonlinear conductivity tensor.

Groups	2SK/2SJ/SSK/Drude	QMD/BSJ/BSK
$\bar{1}', 2'/m$	χ_{xxx} χ_{xyy} χ_{yxx} χ_{yyy}	χ_{yxx} χ_{xyy}
$2/m', m'mm$	χ_{yxx} χ_{yyy}	χ_{yxx}
$\bar{3}'m, \bar{3}'m'$, $6'/mmm'$	$\chi_{yxx} = -\chi_{yyy}$	×
$\bar{3}', 6'/m$	$\chi_{xyy} = -\chi_{xxx}$ $\chi_{yxx} = -\chi_{yyy}$	×

Nonzero nonlinear conductivity elements χ_{abb} on the x-y plane (defined as $J_a = \chi_{abb}E_b^2, \{a,b\} \in \{x,y\}$) for different mechanisms. In 2D, only 9 out of the 122 magnetic point groups [57] have nonzero elements. In 3D, 20 magnetic point groups have nonzero conductivity elements.

transition metal dichalcogenides. One is WTe_2 and the other is $MoTe_2$. In both cases, the nonlinear Hall conductivity is found to arise from both BCD and disorder (SJ and SK) mechanisms. More importantly, our scaling analysis can quantitatively distinguish the BCD contribution from the SJ and SK contributions.

3.2. Strategy and reliability of fitting

To reduce the difficulty of fitting with too many parameters, our strategy is to discard statistically insignificant $\mathscr{C}_n\sigma_{xx}^n$ terms when $|\mathscr{C}_n| < 2\delta_n$, where δ_n is the standard error, because they are statistically indistinguishable from zero within δ_n. After eliminating the insignificant terms, the scaling law can be rewritten in terms of the mechanisms to quantify the ratios of the contributing mechanisms. For $MnBi_2Te_4$ thin films in Fig. 2, the scaling law becomes

$$\chi_{yxx} = \mathscr{C}_{\rm Drude}\sigma_{xx}^2 + \mathscr{C}_{\rm QMD} \tag{4}$$

for the 6 septuple layers, and

$$\begin{aligned}\chi_{yxx} = \ & \mathscr{C}_{\rm 2SK}\left(1-\frac{\sigma_{xx}}{\sigma_{xx0}}\right)^4 + \mathscr{C}_{\rm SSK}\left(1-\frac{\sigma_{xx}}{\sigma_{xx0}}\right)^3 \\ & + \mathscr{C}_{\rm 2SJ}\left(1-\frac{\sigma_{xx}}{\sigma_{xx0}}\right)^2 + \mathscr{C}_{\rm Drude}\sigma_{xx}^2 \\ & + \mathscr{C}_{\rm QMD}\end{aligned} \tag{5}$$

for the 4 septuple layers, respectively. For the 6 septuple layers strained by black phosphorus [10] in Fig. 2a, $\mathscr{C}_{\rm QMD} = 13.3 \pm 0.005$, where the $\pm$ sign gives the standard error. For the 6 septuple layers [54] in Fig. 2c, $\mathscr{C}_{\rm QMD} = (-1.245 \pm 0.079) \times 10^{-1}$ and $\mathscr{C}_{\rm Drude} = (1.725 \pm 0.051) \times 10^{-2}$. For the 6 septuple layers [11] in Fig. 2e, $\mathscr{C}_{\rm QMD} = (-3.74 \pm 0.317) \times 10^3$ and $\mathscr{C}_{\rm Drude} = (5.59 \pm 1.12) \times 10^{-3}$. For the 4 septuple layers [11] in Fig. 2g, $\mathscr{C}_{\rm QMD} = (3.08 \pm 1.77) \times 10^2, \mathscr{C}_{\rm Drude} = (-2.38 \pm 0.765) \times 10^{-2}, \mathscr{C}_{\rm 2SJ} = (1.38 \pm 0.592) \times 10^4, \mathscr{C}_{\rm 2SK} = (7.24 \pm 7.04) \times 10^4$, and $\mathscr{C}_{\rm SSK} = (5.36 \pm 3.51) \times 10^4$. σ_{xx0} is the longitudinal linear conductivity at zero temperature (or the lowest temperature). Similarly, for the $\mathscr{T}$-even cases in Fig. 3, the scaling law reduces to

$$\begin{aligned}\chi_{yxx} = \ & \mathscr{C}_{\rm SK}\sigma_{xx}\left(1-\frac{\sigma_{xx}}{\sigma_{xx0}}\right)^2 + \mathscr{C}_{\rm SJ}\sigma_{xx}\left(1-\frac{\sigma_{xx}}{\sigma_{xx0}}\right) \\ & + \mathscr{C}_{\rm BCD}\sigma_{xx} + \mathscr{C}_{\rm S},\end{aligned} \tag{6}$$

where $\mathscr{C}_{\rm S}$ is a fitting parameter for static scattering [12]. For WTe_2 [6] in Fig. 3a, $\mathscr{C}_{\rm BCD} = 1.01 \pm 0.232, \mathscr{C}_{\rm SJ} = -2.58 \pm 0.378$, and $\mathscr{C}_{\rm S} = 2.35 \pm 1.45$. For $MoTe_2$ [55] in Fig. 3c, $\mathscr{C}_{\rm BCD} = 6.47 \pm 0.347, \mathscr{C}_{\rm SK} = -45.2 \pm 5.64$, and $\mathscr{C}_{\rm SJ} = -8.16 \pm 2.90$. Besides the standard error, the reliability of our fitting results is also quantified by the coefficient of determination R^2 [56], which $\in [0,1]$ and $R^2 = 1$ indicates a perfect fit. For the $MnBi_2Te_4$ thin films, $R^2 = 0.99392$ [54] and 0.88319 [11] for the 6 septuple layers, respectively, and 0.94360 for the 4 septuple layers [11]. For the 6 septuple layers strained by black phosphorus, the $\mathscr{C}_0$ term dominates, so R^2 is not applicable. For WTe_2 and $MoTe_2, R^2 = 0.99836$ and 0.98831, respectively. All the values of R^2 are close to 1, indicating the reliability of the fitting results. Moreover, the procedure is validated by the stability of extracted dominant mechanisms across the conductivity range.

3.3. Symmetry and nonzero nonlinear conductivity elements

The C_3 symmetry addressed in Fig. 2 can be generalized to all magnetic point groups. The point-group symmetries of $\mathscr{T}$-even mechanisms of the second-order nonlinear transport have been addressed in the previous work [14]. Here, we focus on the $\mathscr{T}$-odd mechanisms, which can be classified into three types according to their symmetry properties when exchanging the indices for the input electric fields and output current

$$\begin{aligned}\text{2SK, 2SJ, SSK}: \quad & \chi_{abc} = \chi_{acb}, \\ \text{QMD, BSJ, BSK}: \quad & \chi_{abc} = -\chi_{cba}, \\ \text{Drude}: \quad & \chi_{abc} = \chi_{bca} = \chi_{cab},\end{aligned} \tag{7}$$

where $\{a,b,c\} \in \{x,y,z\}$. We can use the symmetry properties to determine the nonzero nonlinear conductivity elements χ_{abc} for all the crystals classified by the magnetic point groups, as shown in Table 2 for 2D cases. Compared to the point groups, the magnetic point groups [57] can also describe crystals without $\mathscr{T}$ symmetry.

Note that the QMD mechanism [58,59] has fewer nonzero elements than the 2SK, 2SJ, and SSK mechanisms, because of the antisymmetric constraint $\chi_{abc} = -\chi_{cba}$. The unstrained [11] and strained [10] $MnBi_2Te_4$ thin films are classified in the $\bar{3}'m'$ and $2/m'$ magnetic point groups, respectively.

3.4. Experimental implications

Our work suggests several potential future directions. The scaling law in Eq. (3) and Table 1 can be applied to identify mechanisms in future experiments on nonlinear transport. The nonzero elements of nonlinear conductivity in Table 2 can guide future experiments in more materials. The theory can be applied to quantitatively study nonlinear transport in more systems and application scenarios, such as rectification, piezoelectric, and memory devices.

4. Theoretical formulation

4.1. Derivation of nonlinear conductivity formulas

We briefly describe the calculation of the nonlinear conductivity formulas. We start with the uniform Boltzmann equation [12,60]

$$\partial f_l/\partial t + \dot{\mathbf{k}} \cdot \partial f_l/\partial \mathbf{k} = \mathscr{I}_{el}\{f_l\} \tag{8}$$

of the distribution function f_l, where $\mathscr{I}_{el}\{f_l\}$ accounts for the elastic disorder scattering, l stands for the band index γ and wave vector $\mathbf{k}, \dot{\mathbf{k}} = -(e/\hbar)\mathbf{E}$, and $\mathbf{E}$ is the electric field. By decoupling the distribution function and scattering according to different mechanisms (in for disorder-irrelevant, sj and sk for side jump and skew scattering, respectively)

$$\begin{aligned}f_l = \ & f_l^{\rm in} + \delta f_l^{\rm sj} + \delta f_l^{\rm sk} + \delta f_l^{\rm 2sj} \\ & + \delta f_l^{\rm 2sk} + \delta f_l^{\rm sk,sj}, \\ \mathscr{I}_{el}\{f_l\} = \ & \mathscr{I}^{\rm in} + \mathscr{I}^{\rm sj} + \mathscr{I}^{\rm sk} + \mathscr{I}^{\rm sk,sj},\end{aligned} \tag{9}$$

f_l can be found up to the second order of $\mathbf{E}$, where $\delta f_l^{2\mathrm{sj}}+\delta f_l^{2\mathrm{sk}}+\delta f_l^{\mathrm{sk,sj}}$ and $\mathscr{I}^{\mathrm{sk,sj}}$ are crucial for new findings. The nonlinear conductivity χ_{abc} can be extracted from the electric current density $\mathbf{J}(\mathbf{E})=-e\sum_l\dot{\mathbf{r}}_l f_l$, where the velocity

$$\dot{\mathbf{r}}_l=\mathbf{v}_l-\dot{\mathbf{k}}\times(\Omega_l+\nabla_{\mathbf{k}}\times\mathscr{G}\mathbf{E})+\mathbf{v}_l^{\mathrm{sj}} \tag{10}$$

includes the terms from the group velocity $\mathbf{v}_l$, Berry curvature Ω [51], Berry-connection polarizability $\mathscr{G}$, and SJ velocity $\mathbf{v}^{\mathrm{sj}}$.

The nonlinear conductivity formula at second order in Eq. (2) can be decomposed into

$$\begin{aligned}\chi_{abc}=&\sum_{i=1}^{2}\chi_i^{2\mathrm{SK}}+\sum_{i=1}^{3}\chi_i^{2\mathrm{SJ}}+\sum_{i=1}^{4}\chi_i^{\mathrm{SSK}}+\chi^{\mathrm{BSJ}}\\&+\sum_{i=1}^{2}\chi_i^{\mathrm{BSK}}+\chi^{\mathrm{Drude}}+\chi^{\mathrm{QMD}}.\end{aligned} \tag{11}$$

Their explicit forms are given as follows.

$$\chi^{\mathrm{QMD}}=e^2\sum_l\left(v_l^a\mathscr{G}_l^{cb}-v_l^c\mathscr{G}_l^{ab}\right)\partial_{\epsilon_l}f_l^{(0)},$$

as obtained in Refs. [1,8,9,61,62],

$$\chi^{\mathrm{Drude}}=-\frac{\tau^2e^3}{2\hbar^2}\sum_l v_l^a\partial_{\mathbf{k}}^b\partial_{\mathbf{k}}^c f_l^{(0)}, \tag{13}$$

as obtained in Ref. [2],

$$\chi_1^{\mathrm{BSK}}=\frac{\tau^2e^3}{2\hbar^2}\sum_{ll'}\varepsilon^{acd}\Omega_{l'}^d\varpi_{ll'}^{(3A)}\partial_{\mathbf{k}}^b f_l^{(0)}, \tag{14}$$

as obtained in Ref. [33],

$$\chi_2^{\mathrm{BSK}}=\frac{\tau^2e^3}{2\hbar^2}\sum_{ll'}\varepsilon^{acd}\Omega_{l'}^d\varpi_{ll'}^{(4A)}\partial_{\mathbf{k}}^b f_l^{(0)}, \tag{15}$$

$$\chi^{\mathrm{BSJ}}=\frac{\tau e^3}{2\hbar}\sum_l\varepsilon^{acd}\Omega_l^d v_l^{\mathrm{sj},b}\partial_{\epsilon_l}f_l^{(0)}, \tag{16}$$

$$\chi_1^{2\mathrm{SK}}=\frac{e^3\tau^4}{2\hbar^2}\sum_{ll'l''}\left(\partial_{\mathbf{k}''}^c v_{l''}^a\right)\varpi_{l'l}^A\varpi_{l''l'}^A\partial_{\mathbf{k}}^b f_l^{(0)}, \tag{17}$$

$$\chi_2^{2\mathrm{SK}}=\frac{e^3\tau^4}{2\hbar^2}\sum_{ll'l''}v_{l''}^a\left(\partial_{\mathbf{k}}^c-\partial_{\mathbf{k}'}^c\right)\varpi_{l'l}^A\varpi_{l''l'}^A\partial_{\mathbf{k}}^b f_l^{(0)}, \tag{18}$$

$$\chi_1^{2\mathrm{SJ}}=\frac{\tau^2e^3}{2}\sum_{ll'}\left(v_{l'}^a+v_l^a\right)\bar{O}_{l'l}^c v_l^{\mathrm{sj},b}\partial_{\epsilon_l}f_l^{(0)}, \tag{19}$$

$$\chi_2^{2\mathrm{SJ}}=\frac{\tau^2e^3}{2\hbar}\sum_{ll'}\left(v_l^{\mathrm{sj},a}+v_{l'}^{\mathrm{sj},a}\right)\bar{O}_{ll'}^c\partial_{\mathbf{k}}^b f_l^{(0)}, \tag{20}$$

$$\chi_3^{2\mathrm{SJ}}=-\frac{\tau^2e^3}{2\hbar}\sum_l\partial_{\mathbf{k}}^b v_l^{\mathrm{sj},a}v_l^{\mathrm{sj},c}\partial_{\epsilon_l}f_l^{(0)}, \tag{21}$$

$$\chi_1^{\mathrm{SSK}}=\frac{\tau^2e^3}{2\hbar}\sum_{ll'}\left(v_l^a+v_{l'}^a\right)\tilde{O}_{l'l}^c\partial_{\mathbf{k}}^b f_l^{(0)}, \tag{22}$$

$$\chi_2^{\mathrm{SSK}}=\frac{\tau^3e^3}{2\hbar}\sum_{ll'l''}\left(v_{l''}^a+v_{l'}^a\right)\varpi_{ll'}^A\bar{O}_{l''l'}^c\partial_{\mathbf{k}}^b f_l^{(0)}, \tag{23}$$

$$\begin{aligned}\chi_3^{\mathrm{SSK}}=&\frac{\tau^3e^3}{2\hbar}\sum_{ll'l''}\left(\varpi_{l'l}^A+\varpi_{l'l''}^A\right)v_{l'}^a\bar{O}_{ll'}^c\partial_{\mathbf{k}}^b f_l^{(0)}\\&+\frac{\tau^3e^3}{2\hbar}\sum_{ll'}v_{l'}^a v_l^{\mathrm{sj},b}\left(\partial_{\mathbf{k}}^c-\partial_{\mathbf{k}'}^c\right)\varpi_{l'l}^A\partial_{\epsilon_l}f_l^{(0)},\end{aligned} \tag{24}$$

$$\chi_4^{\mathrm{SSK}}=\frac{\tau^3e^3}{2\hbar^2}\sum_{ll'}v_{l'}^{\mathrm{sj},a}\left(\partial_{\mathbf{k}}^c-\partial_{\mathbf{k}'}^c\right)\varpi_{l'l}^A\partial_{\mathbf{k}}^b f_l^{(0)}, \tag{25}$$

where $-e$ is the electron charge, and the scattering time τ is defined as

$$\frac{1}{\tau}\approx\frac{1}{\tau_{\mathbf{k}}}\equiv\sum_{\mathbf{k}'}\varpi_{\mathbf{k}'\mathbf{k}}^{(2)}[1-\cos(\phi-\phi')]\delta(\epsilon_F-\epsilon_l). \tag{26}$$

ε^{abc} is the antisymmetric tensor, and $f_l^{(0)}=\{\exp[(\epsilon_l-\epsilon_F)/k_BT]+1\}^{-1}$ is the Fermi distribution, where ϵ_F is the Fermi energy, k_B is the Boltzmann constant, and T is the temperature. The composite index $l=(\gamma,\mathbf{k})$ denotes a state specified by the band index γ and, in 2D, the wave vector $\mathbf{k}=|\mathbf{k}|(\cos\phi,\sin\phi)$. Following Ref. [51], the Berry curvature is defined as

$$\Omega_l^a\equiv-2\varepsilon^{abc}\sum_{\gamma'\neq\gamma}\frac{\mathrm{Im}\langle\gamma|\partial_{\mathbf{k}}^b\hat{\mathscr{H}}|\gamma'\rangle\langle\gamma'|\partial_{\mathbf{k}}^c\hat{\mathscr{H}}|\gamma\rangle}{\left(\epsilon_{\mathbf{k}}^\gamma-\epsilon_{\mathbf{k}}^{\gamma'}\right)^2}. \tag{27}$$

$\partial_{\mathbf{k}}^b\equiv\partial/\partial k_b$, $\hat{\mathscr{H}}$ is the Hamiltonian, and ϵ_l is the eigenenergy. The group velocity is $v_l^a=(1/\hbar)\partial\epsilon_l/\partial k_a$, and $\partial_{\epsilon_l}\equiv\partial/\partial\epsilon_l$. The factor $\partial_{\epsilon_l}f_l^{(0)}$ restricts the response to states near the Fermi surface. The side-jump velocity is $v_l^{\mathrm{sj},a}=\sum_{l'}\varpi_{ll'}^S\delta r_{l'l}^a$. The quantities $\varpi_{ll'}^S$ and $\varpi_{l'l}^A$) denote the symmetric and antisymmetric scattering rates, respectively, between states l and l'. The coordinate shift is defines

$$\delta r_{ll'}^a\equiv i\langle l|\partial_{\mathbf{k}}^a|l\rangle-i\langle l'|\partial_{\mathbf{k}'}^a|l'\rangle-\left(\partial_{\mathbf{k}}^a+\partial_{\mathbf{k}'}^a\right)\arg(V_{ll'}). \tag{28}$$

The disorder matrix element is $V_{ll'}=\left\langle l|\hat{V}_{imp}|l'\right\rangle$ [12,60]. For the δ-correlated random potential $\hat{V}_{imp}(\mathbf{r})=\sum_iV_i\delta(\mathbf{r}-\mathbf{R}_i)$, the Gaussian and non-Gaussian disorder correlations are $\left\langle V_i^2\right\rangle_{dis}=V_0^2$ and $\left\langle V_i^3\right\rangle_{dis}=V_1^3$, respectively [12,14,60]. These correlations give rise to the intrinsic and extrinsic skew-scattering rates, $\varpi_{l'l}^{(4A)}$ and $\varpi_{l'l}^{(3A)}$, respectively, such that

$$\varpi_{l'l}^A=\varpi_{l'l}^{3A}+\varpi_{l'l}^{4A}. \tag{29}$$

$\bar{O}_{ll'}^a$ ($\tilde{O}_{ll'}^a$) is the symmetric (antisymmetric) part of [12]

$$O_{ll'}^a\equiv(2\pi/\hbar)|T_{ll'}|^2\delta r_{ll'}^a\partial_{\epsilon_l}\delta(\epsilon_l-\epsilon_{l'}), \tag{30}$$

and $T_{ll'}$ is the T-matrix [63]. Alternatively, the calculation can be based on the density matrix [49,64,65]. Their hierarchy and physical pictures are illustrated in Fig. 1. These conductivity formulas are also given in Ref. [50].

4.2. Nonlinear conductivity of QMD

In the nonlinear conductivity formula of the QMD mechanism χ^{QMD} given above, the Berry connection polarizability tensor reads [1,8,9]

$$\mathscr{G}_{\gamma,\mathbf{k}}^{ab}\equiv2e\mathrm{Re}\sum_{\gamma'\neq\gamma}A_{a,\mathbf{k}}^{\gamma\gamma'}A_{b,\mathbf{k}}^{\gamma'\gamma}/\left(\epsilon_{\mathbf{k}}^\gamma-\epsilon_{\mathbf{k}}^{\gamma'}\right). \tag{31}$$

The corresponding quantum metric tensor is given by [37,38]

$$g_{\gamma,\mathbf{k}}^{ab}\equiv\mathrm{Re}\sum_{\gamma\neq\gamma'}A_{a,\mathbf{k}}^{\gamma\gamma'}A_{b,\mathbf{k}}^{\gamma'\gamma}, \tag{32}$$

where the Berry connection $A_{a,\mathbf{k}}^{\gamma\gamma'}\equiv i\langle\gamma|\partial_{\mathbf{k}}^a|\gamma'\rangle$ [51]. For two-band systems, they are explicitly related as

$$\mathscr{G}_{\gamma,\mathbf{k}}^{ab}=2eg_{\gamma,\mathbf{k}}^{ab}/\left(\epsilon_{\mathbf{k}}^\gamma-\epsilon_{\mathbf{k}}^{\gamma'}\right). \tag{33}$$

4.3. Symmetry of nonlinear conductivity formulas

In Eq. (31), the velocity v is odd under both $\mathscr{T}$ and $\mathscr{P}$ operations, while the Berry curvature polarizability $\mathscr{G}$ is even under both $\mathscr{T}$ and $\mathscr{P}$ operations, so $v\mathscr{G}$ is odd under both $\mathscr{T}$ and $\mathscr{P}$ operations but even under the joint $\mathscr{PT}$ symmetry. Therefore, to have a non-

Table 3
Symmetry properties of quantities in nonlinear conductivity formulas.

	∂_a	v_l^a	Ω_l^a	$\delta r_{ll'}^a$	$v_{a,l}^{\mathrm{sj}}$	$\overline{O}_{ll'}^a$	$\widetilde{O}_{ll'}^a$	$\varpi_{ll'}^S$	$\varpi_{ll'}^A$
$\mathscr{P}$	−	−	+	−	−	−	−	+	+
$\mathscr{T}$	−	−	−	+	+	+	−	+	−
$\mathscr{PT}$	+	+	−	−	−	−	+	+	−

The symbols − and + indicate that the corresponding quantity changes sign and remains invariant, respectively, under the indicated symmetry operation.

zero χ^{QMD}, both the $\mathscr{T}$ and $\mathscr{P}$ must be broken, while χ^{QMD} can survive the $\mathscr{PT}$ symmetry. We can use Table 3 to check that all formulas given above have the same symmetries as χ^{QMD}.

Take the formula of χ_4^{SSK} given above for example, in which $v_{l'}^{\mathrm{sj},a}(\partial_{\mathbf{k}}^c - \partial_{\mathbf{k}'}^c)\varpi_{l'l}^A\partial_{\mathbf{k}}^b$ gives $(-1)\ (-1)\ (+1)\ (-1) = -1$ upon $\mathscr{P}$, $(+1)\ (-1)\ (-1)\ (-1) = -1$ upon $\mathscr{T}$, and $(-1)\ (+1)\ (-1)\ (+1) = 1$ under the joint $\mathscr{PT}$ operation, so it has the same symmetry of χ^{QMD}. The symmetry of the other formulas can be shown similarly.

5. Conclusion

In conclusion, we have established a unified framework that treats quantum geometry and disorder-induced mechanisms on an equal footing in second-order nonlinear transport. By systematically enumerating the relevant mechanisms, we derived a polynomial scaling law whose distinct weight distributions provide quantitative fingerprints for separating the quantum metric dipole and Berry curvature dipole contributions from disorder backgrounds. Applications to existing experiments with and without time-reversal symmetry demonstrate that the framework can identify and quantify the dominant mechanisms. We also use a magnetic-point-group analysis to determine the allowed nonlinear conductivity elements. Together with the explicit conductivity formulas, these results provide an experimentally implementable workflow for extracting quantum-geometric contributions from nonlinear-transport measurements and for guiding future material and device studies.

Conflict of interest

The authors declare that they have no conflict of interest.

Author contributions

Zhen–Hao Gong did the calculations with assistance from Z.Z. Du, Hai-Peng Sun, and Hai-Zhou Lu; Zhen–Hao Gong, Z.Z. Du, and Hai-Zhou Lu wrote the manuscript with assistance from Hai-Peng Sun and X.C. Xie; Hai-Zhou Lu and X.C. Xie supervised the project.

Acknowledgements

This work was supported by the National Key R&D Program of China (2022YFA1403700), the Quantum Science and Technology–National Science and Technology Major Project (2021ZD0302400), the National Natural Science Foundation of China (12525401, 12350402, and 12374041), Guangdong Basic and Applied Basic Research Foundation (2023B0303000011), Guangdong Provincial Quantum Science Strategic Initiative (GDZX2201001 and GDZX2401001), the Science, Technology and Innovation Commission of Shenzhen Municipality (ZDSYS20190902092905285), the High-level Special Funds (G03050K004), the New Cornerstone Science Foundation through the XPLORER PRIZE, and the Center for Computational Science and Engineering of SUSTech. We thank Xiangang Wan and Xiaoqun Wang for helpful discussions.

Appendix A. Supplementary material

Supplementary data to this article can be found online at https://doi.org/10.1016/j.scib.2026.07.062.

References

[1] Gao Y, Yang SA, Niu Q. Field induced positional shift of Bloch electrons and its dynamical implications. Phys Rev Lett 2014;112:166601.
[2] Sodemann I, Fu L. Quantum nonlinear Hall effect induced by Berry curvature dipole in time-reversal invariant materials. Phys Rev Lett 2015;115:216806.
[3] Low T, Jiang Y, Guinea F. Topological currents in black phosphorus with broken inversion symmetry. Phys Rev B 2015;92:235447.
[4] Ma Q, Xu SY, Shen H, et al. Observation of the nonlinear Hall effect under time-reversal-symmetric conditions. Nature 2019;565:337–42.
[5] Du ZZ, Wang CM, Lu HZ, et al. Band signatures for strong nonlinear Hall effect in bilayer WTe_2. Phys Rev Lett 2018;121:266601.
[6] Kang K, Li T, Sohn E, et al. Observation of the nonlinear anomalous Hall effect in few-layer WTe_2. Nat Mater 2019;18:324–8.
[7] Du ZZ, Lu HZ, Xie XC. Nonlinear Hall effects. Nat Rev Phys 2021;3:744–52.
[8] Wang C, Gao Y, Xiao D. Intrinsic nonlinear Hall effect in antiferromagnetic tetragonal CuMnAs. Phys Rev Lett 2021;127:277201.
[9] Liu H, Zhao J, Huang YX, et al. Intrinsic second-order anomalous Hall effect and its application in compensated antiferromagnets. Phys Rev Lett 2021;127:277202.
[10] Gao A, Liu YF, Qiu JX, et al. Quantum metric nonlinear Hall effect in a topological antiferromagnetic heterostructure. Science 2023;381:181–6.
[11] Wang N, Kaplan D, Zhang Z, et al. Quantum-metric-induced nonlinear transport in a topological antiferromagnet. Nature 2023;621:487–92.
[12] Du ZZ, Wang CM, Li S, et al. Disorder-induced nonlinear Hall effect with time-reversal symmetry. Nat Commun 2019;10:3047.
[13] Xiao C, Du ZZ, Niu Q. Theory of nonlinear Hall effects: modified semiclassics from quantum kinetics. Phys Rev B 2019;100:165422.
[14] Du ZZ, Wang CM, Sun HP, et al. Quantum theory of the nonlinear Hall effect. Nat Commun 2021;12:5038.
[15] Tiwari A, Chen F, Zhong S, et al. Giant *c*-axis nonlinear anomalous Hall effect in T_d-$MoTe_2$ and WTe_2. Nat Commun 2021;12:2049.
[16] Duan J, Jian Y, Gao Y, et al. Giant second-order nonlinear Hall effect in twisted bilayer graphene. Phys Rev Lett 2022;129:186801.
[17] Sinha S, Adak PC, Chakraborty A, et al. Berry curvature dipole senses topological transition in a moiré superlattice. Nat Phys 2022;18:765–70.
[18] Kaplan D, Holder T, Yan B. General nonlinear Hall current in magnetic insulators beyond the quantum anomalous Hall effect. Nat Commun 2023;14:3053.
[19] Min L, Tan H, Xie Z, et al. Strong room-temperature bulk nonlinear Hall effect in a spin-valley locked Dirac material. Nat Commun 2023;14:364.
[20] Jin Z, Yao X, Wang Z, et al. Nonlinear topological magnon spin Hall effect. Phys Rev Lett 2023;131:166704.
[21] Yokouchi T, Ikeda Y, Morimoto T, et al. Giant magnetochiral anisotropy in Weyl semimetal WTe_2 induced by diverging Berry curvature. Phys Rev Lett 2023;130:136301.
[22] Huang M, Wu Z, Zhang X, et al. Intrinsic nonlinear Hall effect and gate-switchable Berry curvature sliding in twisted bilayer graphene. Phys Rev Lett 2023;131:066301.
[23] Fang Y, Cano J, Ghorashi SAA. Quantum geometry induced nonlinear transport in altermagnets. Phys Rev Lett 2024;133:106701.
[24] Suárez-Rodríguez M, Martín-García B, Skowroski W, et al. Odd nonlinear conductivity under spatial inversion in chiral tellurium. Phys Rev Lett 2024;132:046303.
[25] Kaplan D, Holder T, Yan B. Unification of nonlinear anomalous Hall effect and nonreciprocal magnetoresistance in metals by the quantum geometry. Phys Rev Lett 2024;132:026301.
[26] Chen R, Du ZZ, Sun HP, et al. Nonlinear Hall effect on a disordered lattice. Phys Rev B 2024;110:L081301.
[27] He P, Isobe H, Koon GKW, et al. Third-order nonlinear Hall effect in a quantum Hall system. Nat Nanotechnol 2024;19:1460–5.
[28] Wang E, Zeng H, Duan W, et al. Spontaneous inversion symmetry breaking and emergence of Berry curvature and orbital magnetization in topological $ZrTe_5$ films. Phys Rev Lett 2024;132:266802.
[29] Makushko P, Kovalev S, Zabila Y, et al. A tunable room-temperature nonlinear Hall effect in elemental bismuth thin films. Nat Electron 2024;7:207–15.

[30] Lihm JM, Park CH. Nonlinear Hall effect from long-lived valley-polarizing relaxons. Phys Rev Lett 2024;132:106402.
[31] Isobe H, Xu SY, Fu L. High-frequency rectification via chiral Bloch electrons. Sci Adv 2020;6:eaay2497.
[32] Kumar D, Hsu CH, Sharma R, et al. Room-temperature nonlinear Hall effect and wireless radiofrequency rectification in Weyl semimetal $TaIrTe_4$. Nat Nanotechnol 2021;16:421–5.
[33] Ma D, Arora A, Vignale G, et al. Anomalous skew-scattering nonlinear Hall effect and chiral photocurrents in $\mathscr{PT}$-symmetric antiferromagnets. Phys Rev Lett 2023;131:076601.
[34] Ghosh B, Onishi Y, Xu SY, et al. Probing quantum geometry through optical conductivity and magnetic circular dichroism. Sci Adv 2024;10:eado1761.
[35] Shin D, Rubio A, Tang P. Light-induced ideal Weyl semimetal in HgTe via nonlinear phononics. Phys Rev Lett 2024;132:016603.
[36] Hu J, Li W, Guo Z, et al. Quantum geometry in phonon-mediated optical responses. Phys Rev Lett 2025;135:256404.
[37] Provost J, Vallee G. Riemannian structure on manifolds of quantum states. Commun Math Phys 1980;76:289–301.
[38] Resta R. The insulating state of matter: a geometrical theory. Eur Phys J B 2011;79:121–37.
[39] Parameswaran SA, Roy R, Sondhi SL. Fractional Chern insulators and the W_∞ algebra. Phys Rev B 2012;85:241308.
[40] Roy R. Band geometry of fractional topological insulators. Phys Rev B 2014;90:165139.
[41] Peotta S, Törmä P. Superfluidity in topologically nontrivial flat bands. Nat Commun 2015;6:8944.
[42] Törmä P, Peotta S, Bernevig BA. Superconductivity, superfluidity and quantum geometry in twisted multilayer systems. Nat Rev Phys 2022;4:528–42.
[43] Törmä P. Essay: where can quantum geometry lead us? Phys Rev Lett 2023;131:240001.
[44] Hetényi B, Lévay P. Fluctuations, uncertainty relations, and the geometry of quantum state manifolds. Phys Rev A 2023;108:032218.
[45] Hu J, Li W, Wang H, et al. Phonon-mediated nonlinear optical responses and quantum geometry. arXiv:2410.09677; 2024.
[46] Liu T, Qiang XB, Lu HZ, et al. Quantum geometry in condensed matter. Natl Sci Rev 2025;12:nwae334.
[47] Gong M, Zhao PL, Lu HZ, et al. Emergence of nodal-knot transitions by disorder. Sci Bull 2025;70:2088–93.
[48] Nagaosa N, Sinova J, Onoda S, et al. Anomalous Hall effect. Rev Mod Phys 2010;82:1539–92.
[49] Atencia RB, Xiao D, Culcer D. Disorder in the nonlinear anomalous Hall effect of $\mathscr{PT}$-symmetric Dirac fermions. Phys Rev B 2023;108:L201115.
[50] Huang YX, Xiao C, Yang SA, et al. Scaling law and extrinsic mechanisms for time-reversal-odd second-order nonlinear transport. Phys Rev B 2025;111:155127.
[51] Xiao D, Chang MC, Niu Q. Berry phase effects on electronic properties. Rev Mod Phys 2010;82:1959–2007.
[52] Tian Y, Ye L, Jin X. Proper scaling of the anomalous Hall effect. Phys Rev Lett 2009;103:087206.
[53] Hou D, Su G, Tian Y, et al. Multivariable scaling for the anomalous Hall effect. Phys Rev Lett 2015;114:217203.
[54] Gao A, Chen SW, Ghosh B, et al. An antiferromagnetic diode effect in even-layered $MnBi_2Te_4$. Nat Electron 2024;7:751–9.
[55] Ma T, Chen H, Yananose K, et al. Growth of bilayer $MoTe_2$ single crystals with strong non-linear Hall effect. Nat Commun 2022;13:5465.
[56] Steel RGD, Torrie JH. Principles and procedures of statistics: with special reference to the biological sciences. New York: McGraw-Hill; 1960.
[57] Litvin DB. Magnetic group tables. Chester, England: International Union of Crystallography; 2013.
[58] Zhang ZF, Zhu ZG, Su G. Symmetry dictionary on charge and spin nonlinear responses for all magnetic point groups with nontrivial topological nature. Natl Sci Rev 2023;10:nwad104.
[59] Zhu H, Li J, Chen X, et al. Magnetic geometry induced quantum geometry and nonlinear transports. Nat Commun 2025;16:4882.
[60] Sinitsyn NA. Semiclassical theories of the anomalous Hall effect. J Phys Condens Matter 2008;20:023201.
[61] Xiao C, Cao J, Niu Q, et al. Proper definition of intrinsic nonlinear current. Phys Rev Lett 2025;135:256306.
[62] Qiang XB, Liu T, Gao ZX, et al. A clarification on quantum-metric-induced nonlinear transport. Adv Sci 2026;13:e14818.
[63] Mahan GD. Many-particle physics. New York: Springer; 2013.
[64] Atencia RB, Niu Q, Culcer D. Semiclassical response of disordered conductors: extrinsic carrier velocity and spin and field-corrected collision integral. Phys Rev Res 2022;4:013001.
[65] Mehraeen M. Quantum kinetic theory of quadratic responses. Phys Rev B 2024;110:174423.